Featured in Physics

Holographic Plasma Lenses

M. R. Edwards[,1,*] V. R. Munirov,[2] A. Singh,[2] N. M. Fasano,[3] E. Kur,[1] N. Lemos,[1]
J. M. Mikhailova,[3] J. S. Wurtele,[2] and P. Michel[1]

[1]*Lawrence Livermore National Laboratory, Livermore, California 94550, USA*
[2]*University of California at Berkeley, Berkeley, California 94720, USA*
[3]*Princeton University, Princeton, New Jersey 08544, USA*

A hologram fully encodes a three-dimensional light field by imprinting the interference between the field and a reference beam in a recording medium. Here we show that two collinear pump lasers with different foci overlapped in a gas jet produce a holographic plasma lens capable of focusing or collimating a probe laser at intensities several orders-of-magnitude higher than the limits of a nonionized optic. We outline the theory of these diffractive plasma lenses and present simulations for two plasma mechanisms that allow their construction: spatially varying ionization and ponderomotively driven ion-density fluctuations. Damage-resistant plasma optics are necessary for manipulating high-intensity light, and divergence control of high-intensity pulses—provided by holographic plasma lenses—will be a critical component of high-power plasma-based lasers.

Holograms record both the phase and the amplitude of light, allowing the complete reconstruction of a light field at a later time [1]. A hologram is created by imprinting the interference between a signal beam and a reference beam in a light-sensitive medium, e.g., a photographic plate; a delayed second reference beam diffracts to reproduce the signal beam. The interference is commonly mapped to attenuation, but the pattern may also be embedded as a phase shift [2]: a variation of the refractive index's real component. Any medium where the index of refraction is modified by the intensity of light can be used, but current holograms rely on a limited collection of solid-state materials. The index of refraction (n) of a plasma ($n < 1$) differs from that of both vacuum ($n = 1$) and neutral gas at similar density ($n > 1$), and the formation and density evolution of plasma may be driven by light. We may therefore create a hologram using lasers to modulate plasma density.

The damage threshold of a plasma is orders-of-magnitude higher than that of a solid-state optic; plasma optics use this to manipulate light at extreme intensities [3]. Plasma-based versions of optical components include amplifiers [4–7], gratings [8–11], mirrors [12,13], wave plates [14–16], and Pockels cells [17]. However, the only demonstrated solutions for focusing light with unfocused intensity above 10^{12} W/cm^2 are the concave plasma mirror [18] and compound parabolic concentrator [19], neither of which is well-suited to high-repetition-rate experiments. A holographic plasma lens offers an alternative approach. Imprinting the interference between two copropagating pump beams with different foci in a plasma (e.g., a collimated beam and a tightly focused one) results in a

plasma-based zone plate, a diffractive lens which in non-plasma form is used to focus x rays [20]. An efficient holographic plasma lens could allow collimation of high-intensity light for high-order harmonic generation [21] and filamentation [22] experiments or improve the focusing of high-energy laser facilities (e.g., the Advanced Radiographic Capability (ARC) laser [23]). Previous efforts to design plasma holograms have relied on reflective surface [24] and reflective volume [25] approaches, which require high-quality surfaces and high (near-solid) plasma density, restricting viability for high-repetition-rate systems, or electron plasma waves [26], which are short-lived and are destroyed when the probe intensity is comparable to that of the pump beams, a serious constraint for a plasma optic.

In this Letter, we propose a new plasma lens concept based on transmission volume holograms constructed via two plausible plasma mechanisms: spatially varying ionization (SVI) or ponderomotively driven ion structures. Both schemes rely on two copropagating pump beams whose interference pattern imprints a three-dimensional (3D) refractive index structure acting as a diffractive lens. SVI uses ionization of a background gas in the high-intensity fringes of the interference pattern while areas of destructive interference remain as neutral gas, leading to an index modulation $n_{gas} - n_{plasma} \approx 10^{-2}$ [27–30]. For ponderomotively driven structures, electrons are ponderomotively forced out of high-intensity regions; the resultant space-charge force pulls ions down the intensity gradients as well. An index modulation is then formed by the plasma density difference between the high and low intensity regions [8–10,31–33]. For both mechanisms, the diffractive lens structure remains after the pumps are turned off. The
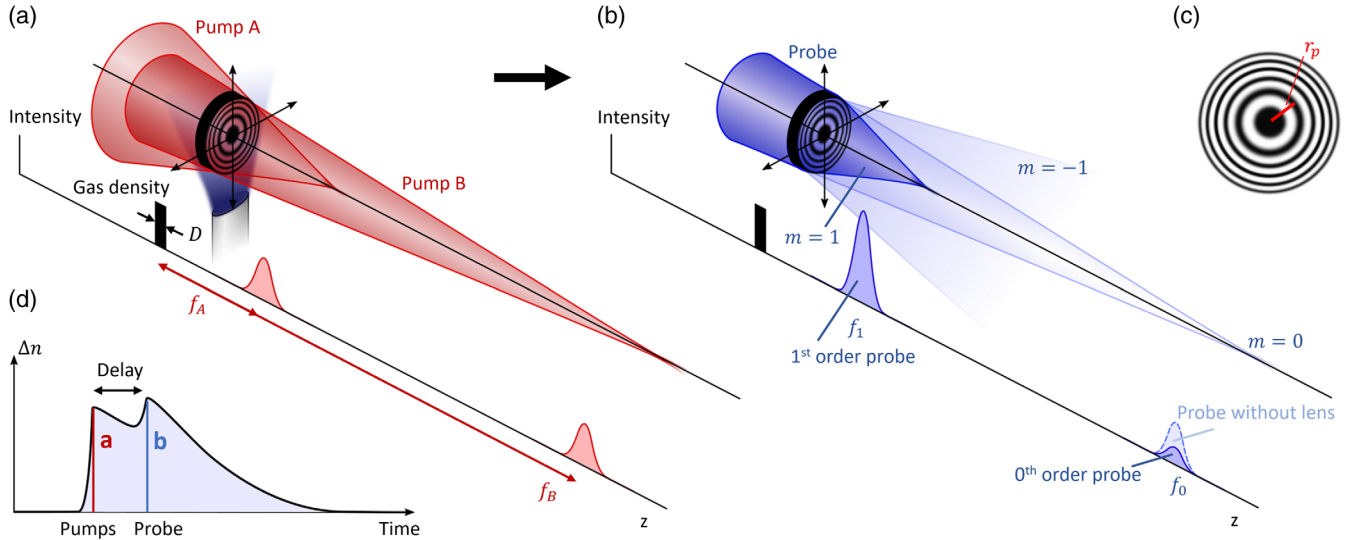
FIG. 1.   Schematic of a holographic plasma lens. (a) Two pump lasers overlap in a gas (extent along z is D), arranged so that their interference pattern is a sinusoidal zone plate. (b) At a delayed time, a probe laser passes through the resulting structure and is diffracted into one or more orders. (c) The intensity profile of the overlapped pumps and the resultant index modulation. (d) The peak index of refraction modulation as a function of time, showing the formation of the structure with the arrival of the pumps, followed by a decay and possible modification by the probe. The amplitude and timescale both depend on the chosen nonlinear mechanism.

relaxation time is dictated by recombination and diffusion for SVI [29] and by ion motion for ponderomotive structures [10]. This enables the manipulation of a probe at a substantial delay or with a much longer duration than the pump lasers, and, as we show here, requires relatively small volumes of gas-density plasma to create efficient transmission holograms tolerating probe intensities from 10^{14} to 10^{17} W/cm^2.

Consider two collinear equal-power pump lasers ($\alpha = A$, B) focused at distinct points f_α along z with the f number of each beam (F_α) chosen such that they have the same beam diameter at $z = 0$ ($|f_A/F_A| = |f_B/F_B|$), as shown in Fig. 1(a). The beams propagate in vacuum outside a region with extent D centered at $z = 0$ where the index of refraction is intensity dependent, a configuration that can, for example, be realized with a gas jet. For ease of analysis, we will restrict f_α to be larger than the Rayleigh range. The two pumps interfere everywhere they overlap, but inside the gas that interference is encoded as a variation of the refractive index by the dependence of n on intensity (I), creating the index modulation of a zone plate [Fig. 1(c)]. At a delayed time [Fig. 1(d)], a probe crossing the index modulation can be focused [Fig. 1(b)], with the plasma density potentially evolving due to both the pumps and the probe.

A zone plate consists of concentric alternating regions of opaque or phase shifting material, spaced so that transmitted light interferes constructively at the desired focal point [2,34,35]. The radii of boundaries between zones (r_p for the pth boundary) are associated with $\lambda/2$ phase shifts of light, from which follows $r_p^2 = p\lambda(f + p\lambda/4)$, λ is the wavelength of the light of interest, and f is the focal length. For $p\lambda \ll f$, $r_p^2 \approx p\lambda f$. If the pump and probe have different wavelengths (λ_p and λ_0, respectively), both must satisfy $p\lambda \ll f$ for efficient diffraction. The size of the focal spot is governed by the total number of zones (P) as $w_0 = \sqrt{\lambda f/4P}$, which follows from the dependence of spot size on numerical aperture. Zone plates are highly chromatic, restricting the focusable bandwidth ($\Delta\lambda$); the probe must satisfy $\Delta\lambda/\lambda_0 \leq 1/P$ for the focal position of its component wavelengths to differ by no more than a Rayleigh range.

A zone plate created by two pump lasers with focal spots at f_A and f_B will have focal length

$$f = \frac{f_A f_B}{f_A - f_B} \cdot \frac{\lambda_p}{\lambda_0}. \tag{1}$$

A probe focused at the point f_0 along the z axis, will, after passing through the plasma zone plate, have new m-order focal spots at

$$f_m = \frac{f f_0}{f + m f_0}, \tag{2}$$

where f is given by Eq. (1) and the energy in each order is determined by the detailed spatial variation of the refractive index [36].

We can distinguish two regimes for diffractive lenses by the thickness of the optic relative to the light wavelength and zone size. For a thin lens ($Q = D\lambda_0/\delta^2 \ll 1$, where δ is the width of the outer-most zone), the thickness of the optic is set by the condition that adjacent zones produce a relative phase shift of π: $\Delta\phi \approx \pi = 2\pi(D/\lambda_0)\Delta n$. For a volumetric (thick) plasma lens ($Q \gg 1$), which can be described by coupled mode theory [47], the required thickness is [48]

$$\frac{D}{\lambda_0} \approx \frac{1}{\Delta n}. \tag{3}$$

Taking SVI as a representative example, we will neglect absorption and note that the real part of the refractive index varies between that for plasma ($n = \sqrt{1 - n_e/n_c}$ where n_e is the plasma density and n_c is the plasma critical density $n_c = \varepsilon_0 m_e \omega^2/e^2$) and that for the nonionized gas, where ordinarily $|1 - n_{\text{plasma}}| \gg |1 - n_{\text{gas}}|$. A reasonable approximation is then $\Delta n \approx 1 - n_{\text{plasma}} = 1 - \sqrt{1 - n_e/n_c} \approx n_e/2n_c$ for $n_e \ll n_c$. From this and the above condition on $\Delta\phi$, the plasma density and thickness should satisfy $n_e D/2n_c \approx \lambda_0$.

Thin lenses support multiple diffraction orders, whereas a thick lens can produce a single well-defined spot [47]. This is analogous to the Raman-Nath and Bragg regimes for diffraction gratings. The loss of energy to higher orders for thin lenses makes them less attractive as focusing optics, and here we will focus on the thick lens regime, using three types of simulation to study the interaction: a linear paraxial solver, a nonlinear paraxial solver, and a particle-in-cell code.

First, we use a linear 3D paraxial propagation solver (PPS) to numerically evaluate the formation and performance of diffractive lens shapes. The solver neglects the time dynamics of the pumps and probe and considers the interaction as three separate steps: (1) linear propagation of the pumps through a uniform medium, (2) change of the refractive index as a function of pump intensity, and (3) linear propagation of the probe through the new distribution of refractive index [36]. The arbitrary functional relationship between the pump intensity and the refractive index in step (2) allows both SVI and ponderomotive lenses to be approximated. Figure 2(a) shows a probe beam with vacuum focus at $z = 1$ mm being collimated by a thick plasma lens, with 80% of the energy within the (collimated) $m = -1$ mode. In Fig. 2(b), a similar plasma lens focuses a collimated incident probe, with more than 50% of the energy inside a 2 μm spot. Figure 2(c) shows how the focusing efficiency of the optic in (b) decreases as the plasma density changes from its
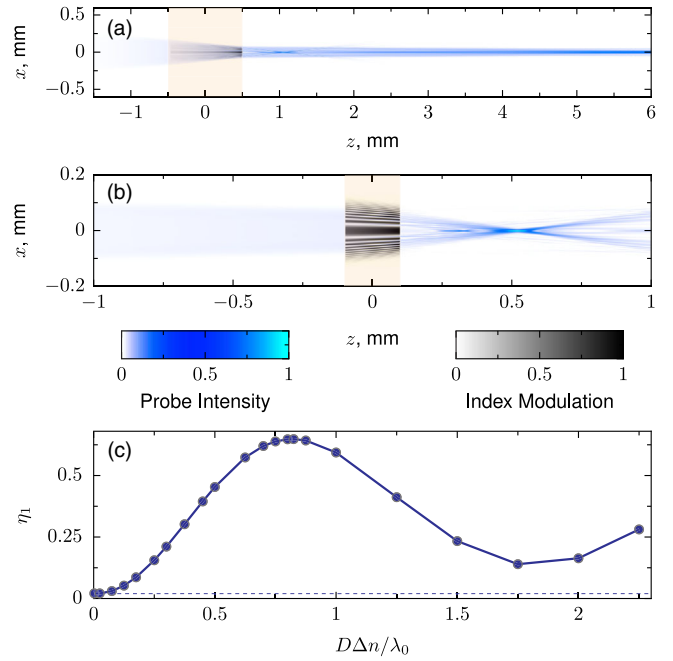

FIG. 2. Calculations (3D PPS) for a thick plasma lens, showing collimation (a) and focusing (b) depending on the initial probe focus position. (a) Probe (blue) near-collimated to focus at $z = 6$ mm by lens formed in $D = 1$ mm initial gas (orange), with $\Delta n = 1.3 \times 10^{-4}$, $\lambda_p = \lambda_0 = 400$ nm, $f_A = 1$ mm, and $f_B = 6$ mm; 81% of energy is within the focal spot at $z = 6$ mm. (b) Focusing lens with $D = 200$ μm and $\Delta n = 3.3 \times 10^{-3}$ for $\lambda_0 = 800$ nm probe. Focal spot full-width-half-maximum is 2.2 μm. Pumps have $\lambda_p = 800$ nm, $f_A = 0.5$ mm, and $f_B = 3$ mm. (c) Efficiency (η_1) for lens shown in (b), defined as probe energy a within 10-μm radius at $z = 0.5$ mm as Δn is varied between 1×10^{-5} and 9×10^{-3} for fixed D.

optimal value. The maximum efficiency occurs near where $D/\lambda_0 = \Delta n$, with smaller values of $D\Delta n/\lambda_0$ producing minimal energy transfer to the $m = 1$ order.

To capture the nonlinear dynamics of SVI, where high-intensity pulses propagate in an initially neutral gas, we use a 3D numerical envelope equation solver [49] with governing equation [40]:

$$\frac{\partial E}{\partial z} = \frac{i}{2k}\nabla_\perp^2 E - \frac{ik''}{2}\frac{\partial^2 E}{\partial t^2} - \frac{\sigma}{2}(1 + i\omega\tau)n_e E - W_{\text{FI}}(E)n_N\frac{U_i}{2|E|^2} + ik_0 n_2^T\left[(1 - f)|E|^2 + f\int_{-\infty}^{\infty} R(t - t')|E(t')|^2 dt'\right] \tag{4}$$

where k is the wave number, σ is the inverse Bremsstrahlung cross section, τ is the collision time, W_{FI} is the field ionization rate, n_N is the neutral density, U_i is the ionization energy, n_2^T is the total Kerr nonlinearity with f the time delayed fraction, and $R(t)$ is a damped harmonic oscillator model for the delayed response [36]. The terms on the right-hand side describe diffraction, group velocity dispersion, plasma phase shift and absorption, ionization losses, and Kerr self-focusing, respectively. The evolution of the plasma due to field and collisional ionization and recombination is separately calculated. Figures 3(a) and 3(b) show the results from a simulation of a 170 μm diameter ionization lens formed in a 2 mm nitrogen gas column by two 0.65 mJ, 10 fs pumps. In Fig. 3(a), the free
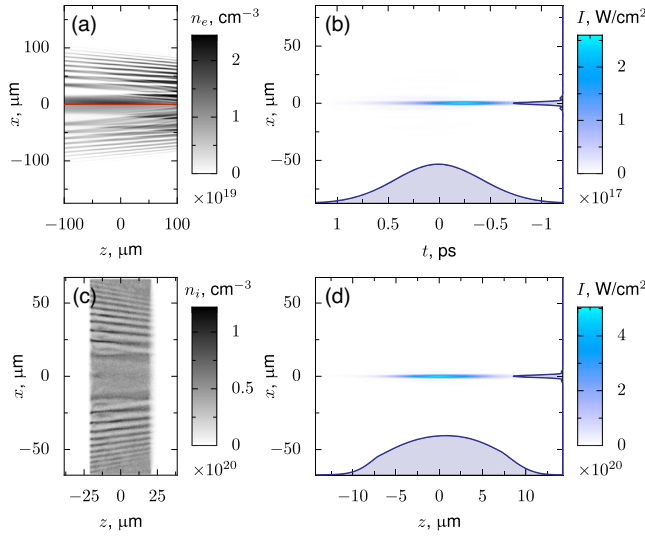
FIG. 3. Simulations of focusing by thick plasma lenses formed by SVI [(a),(b)] and ion fluctuations [(c),(d)] using a 3D nonlinear envelope equation solver [(a),(b)] and 3D PIC simulations [(c),(d)]. (a) The density of plasma after passage of the pumps (upper half) and the probe (lower half) through a $D = 200~\mu m$ column of molecular nitrogen. (b) The probe intensity at the $z = 3$ mm focal spot. In (a),(b), the pumps are 10 fs, 800 nm, 0.65 mJ pulses focused at $z = 3$ mm and $z = 0.5$ mm, and the probe is 1 ps, 800 nm, and 60 mJ. In (c),(d), the pumps are 15 TW, 1 μm pulses with 500 fs duration, the probe is a 100 TW, 1 μm pulse with 40 fs duration, and the hydrogen plasma has $D = 40~\mu m$ with an initial density density $n_e/n_c = 0.045$ and electron temperature $T_e = 100$ eV. (c) The ion density after both the pump and the probe have passed, and (d) the probe intensity near the focal spot.

electron density left by the pump lasers has the characteristic zone-plate shape. After a delay of 0.8 ps, a 1 ps 60 mJ probe passing through this lens is focused at $z = 0.5$ mm. Slight distortion and a reduction in intensity at the tail end of the probe indicate that this pulse is near the maximum tolerance of the optic, which at 2.4×10^{14} W/cm^2 and 230 J/cm^2 is well above the limits of glass.

A holographic plasma lens can also be created via the ponderomotive force in a fully ionized plasma. As captured by the 3D particle-in-cell (PIC) simulation (using the code EPOCH [50]) shown in Figs. 3(c) and 3(d), the two pump lasers (15 TW, 500 fs duration) ponderomotively create an ion density perturbation in a fully ionized hydrogen plasma [Fig. 3(c)]. Although the pumps are only on for 500 fs, this modulation continues to evolve on a picosecond timescale due to the acquired ion momentum. Under these specific conditions, a 100 TW probe arriving 1.2 ps after the pumps is brought to a high-quality focal spot at $z = 0.2$ mm [Fig. 3(d)]. At this power, the probe closely follows the expected linear behavior based on the index modulation created in the plasma. In fact, as long as the probe is weak enough to not affect the lens, both SVI and ponderomotive optics are well described by the linear PPS code, provided
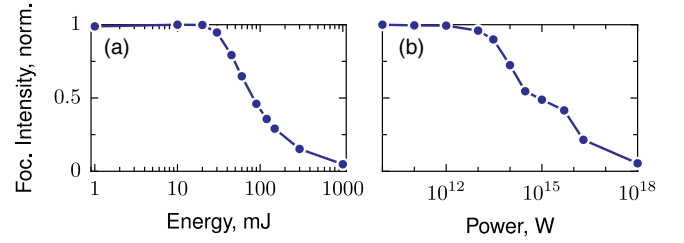

FIG. 4. Plasma lens efficacy (peak focal intensity normalized by incident probe power) at varied incident probe energy for (a) SVI calculated with the 3D nonlinear envelope equation and (b) the ponderomotive ion mechanism using 2D PIC. (a) Parameters apart from probe energy are the same as in Figs. 3(a) and 3(b). (b) Physical parameters are the same as in Figs. 3(c) and 3(d), although these simulations are 2D and the resolution is 20 cells/λ and 10 particles per cell.

that we have an adequate model relating pump intensity to the index modulation. The agreement between PPS and PIC, in particular, suggests that a good understanding of the interaction can be achieved even without fully resolving all components of the electromagnetic fields. However, inclusion of nonlinear effects is required to understand how performance changes as the probe energy increases.

Plasma optics are useful only if they support higher intensity or energy flux in the probe than is required in the pumps that create them, and to be practical, the damage tolerance must be much higher than solid-state equivalents. In Fig. 4(a), 3D nonlinear envelope simulations measure the focusing efficacy, defined here as the peak intensity at focus divided by incident probe power and normalized to the low-power limit, for a SVI lens with the same parameters as in Figs. 3(a) and 3(b). As energy increases to 100 mJ, this efficacy drops, setting an effective damage threshold. At 60 mJ, where performance is above 65%, the probe energy is almost 100 times the energy in each pump and the flux seen by this lens is 230 J/cm^2, well above the energy flux limits for a solid-state optic exposed to a femtosecond pulse. In general, an SVI optic can take advantage of wavelength-dependent ionization or the differences between field and collisional ionization to support higher energy or intensity in the probe than required for the pumps.

A similar approach is used to find an effective damage threshold for a ponderomotive lens, as shown in Fig. 4(b), where 2D PIC simulations at the same conditions as those in Figs. 3(c) and 3(d) capture a gradual drop-off in lens efficacy above 10^{14} W. Near this threshold, the intensity within the lens is more than 10^{17} W/cm^2. A ponderomotive plasma optic relies on the relatively slow response of ions to intense light fields. Although the local electron density provides the index modulation, the plasma lens has an underlying ion density structure which changes shape slowly, helping maintain the overall structure even at high probe intensity. An ion structure can be formed over several

picoseconds by weak pumps, but requires far higher intensity to destroy during the 40 fs probe duration.

In conclusion, we have shown that plasma nonlinearities can be used to create efficient high-damage-threshold diffractive plasma lenses. Simulations suggest that the intensity damage threshold of these lenses ranges from more than 10^{14} W/cm^2 for the ionization mechanism to more than 10^{17} W/cm^2 for the ponderomotive mechanism. The generality of holography means that holographic plasma optics can almost arbitrarily manipulate intense beams; these mechanisms are not limited to the creation of simple lenses.

---

[*]edwards78@llnl.gov

[1] D. Gabor, A new microscopic principle, Nature (London) **161**, 777 (1948).

[2] J. Kirz, Phase zone plates for x rays and the extreme uv, J. Opt. Soc. Am. **64**, 301 (1974).

[3] H. Milchberg, Indestructible plasma optics, Phys. Today **72**, No. 6, 70 (2019).

[4] V. M. Malkin, G. Shvets, and N. J. Fisch, Fast Compression of Laser Beams to Highly Overcritical Powers, Phys. Rev. Lett. **82**, 4448 (1999).

[5] Y. Ping, W. Cheng, S. Suckewer, D. S. Clark, and N. J. Fisch, Amplification of Ultrashort Laser Pulses by a Resonant Raman Scheme in a Gas-Jet Plasma, Phys. Rev. Lett. **92**, 175007 (2004).

[6] A. Andreev, C. Riconda, V. Tikhonchuk, and S. Weber, Short light pulse amplification and compression by stimulated Brillouin scattering in plasmas in the strong coupling regime, Phys. Plasmas **13**, 053110 (2006).

[7] M. R. Edwards, Q. Jia, J. M. Mikhailova, and N. J. Fisch, Short-pulse amplification by strongly-coupled stimulated Brillouin scattering, Phys. Plasmas **23**, 083122 (2016).

[8] P. Michel, L. Divol, E. A. Williams, S. Weber, C. A. Thomas, D. A. Callahan, S. W. Haan, J. D. Salmonson, S. Dixit, D. E. Hinkel, M. J. Edwards, B. J. MacGowan, J. D. Lindl, S. H. Glenzer, and L. J. Suter, Tuning the Implosion Symmetry of ICF Targets Via Controlled Crossed-Beam Energy Transfer, Phys. Rev. Lett. **102**, 025004 (2009).

[9] S. H. Glenzer et al., Symmetric inertial confinement fusion implosions at ultra-high laser energies, Science **327**, 1228 (2010).

[10] G. Lehmann and K. H. Spatschek, Transient Plasma Photonic Crystals for High-Power Lasers, Phys. Rev. Lett. **116**, 225002 (2016).

[11] R. Kirkwood, D. Turnbull, T. Chapman, S. Wilks, M. Rosen, R. London, L. Pickworth, W. Dunlop, J. Moody, D. Strozzi et al., Plasma-based beam combiner for very high fluence and energy, Nat. Phys. **14**, 80 (2018).

[12] C. Thaury, F. Quéré, J.-P. Geindre, A. Levy, T. Ceccotti, P. Monot, M. Bougeard, F. Réau, P. d'Oliveira, P. Audebert, R. Marjoribanks, and Ph. Martin, Plasma mirrors for ultrahigh-intensity optics, Nat. Phys. **3**, 424 (2007).

[13] J. M. Mikhailova, A. Buck, A. Borot, K. Schmid, C. Sears, G. D. Tsakiris, F. Krausz, and L. Veisz, Ultra-high-contrast few-cycle pulses for multipetawatt-class laser technology, Opt. Lett. **36**, 3145 (2011).

[14] P. Michel, L. Divol, D. Turnbull, and J. D. Moody, Dynamic Control of the Polarization of Intense Laser Beams via Optical Wave Mixing in Plasmas, Phys. Rev. Lett. **113**, 205001 (2014).

[15] K. Qu, Q. Jia, and N. J. Fisch, Plasma q-plate for generation and manipulation of intense optical vortices, Phys. Rev. E **96**, 053207 (2017).

[16] D. Turnbull, C. Goyon, G. E. Kemp, B. B. Pollock, D. Mariscal, L. Divol, J. S. Ross, S. Patankar, J. D. Moody, and P. Michel, Refractive Index Seen by a Probe Beam Interacting with a Laser-Plasma System, Phys. Rev. Lett. **118**, 015001 (2017).

[17] D. Turnbull, P. Michel, T. Chapman, E. Tubman, B. B. Pollock, C. Y. Chen, C. Goyon, J. S. Ross, L. Divol, N. Woolsey, and J. D. Moody, High Power Dynamic Polarization Control Using Plasma Photonics, Phys. Rev. Lett. **116**, 205001 (2016).

[18] R. Wilson, M. King, R. Gray, D. Carroll, R. Dance, C. Armstrong, S. Hawkes, R. Clarke, D. Robertson, D. Neely et al., Ellipsoidal plasma mirror focusing of high power laser pulses to ultra-high intensities, Phys. Plasmas **23**, 033106 (2016).

[19] A. G. MacPhee, D. Alessi, H. Chen, G. Cochran, M. R. Hermann, D. H. Kalantar, A. J. Kemp, S. M. Kerr, A. J. Link, T. Ma et al., Enhanced laser–plasma interactions using non-imaging optical concentrator targets, Optica **7**, 129 (2020).

[20] A. Sakdinawat and D. Attwood, Nanoscale x-ray imaging, Nat. Photonics **4**, 840 (2010).

[21] F. Krausz and M. Ivanov, Attosecond physics, Rev. Mod. Phys. **81**, 163 (2009).

[22] A. Couairon and A. Mysyrowicz, Femtosecond filamentation in transparent media, Phys. Rep. **441**, 47 (2007).

[23] J. Crane, G. Tietbohl, P. Arnold, E. Bliss, C. Boley, G. Britten, G. Brunton, W. Clark, J. Dawson, S. Fochs et al., Progress on converting a NIF quad to eight, petawatt beams for advanced radiography, J. Phys. Conf. Ser. **244**, 032003 (2010).

[24] A. Leblanc, A. Denoeud, L. Chopineau, G. Mennerat, P. Martin, and F. Quéré, Plasma holograms for ultrahigh-intensity optics, Nat. Phys. **13**, 440 (2017).

[25] G. Lehmann and K. H. Spatschek, Plasma volume holograms for focusing and mode conversion of ultraintense laser pulses, Phys. Rev. E **100**, 033205 (2019).

[26] I. Y. Dodin and N. J. Fisch, Storing, Retrieving, and Processing Optical Information by Raman Backscattering in Plasmas, Phys. Rev. Lett. **88**, 165001 (2002).

[27] S. Suntsov, D. Abdollahpour, D. Papazoglou, and S. Tzortzakis, Femtosecond laser induced plasma diffraction gratings in air as photonic devices for high intensity laser applications, Appl. Phys. Lett. **94**, 251104 (2009).

[28] L. Shi, W. Li, Y. Wang, X. Lu, L. Ding, and H. Zeng, Generation of High-Density Electrons Based on Plasma Grating Induced Bragg Diffraction in Air, Phys. Rev. Lett. **107**, 095004 (2011).

[29] M. Durand, A. Jarnac, Y. Liu, B. Prade, A. Houard, V. Tikhonchuk, and A. Mysyrowicz, Dynamics of plasma gratings in atomic and molecular gases, Phys. Rev. E **86** (2012).

[30] M. R. Edwards, N. M. Fasano, N. Lemos, A. Singh, V. Munirov, E. Kur, J. S. Wurtele, J. M. Mikhailova, and P. Michel, Measuring the optical properties of ionization gratings in air for control of femtosecond lasers, in *Conference on Lasers and Electro-Optics* (Optical Society of America, 2021), 10.1364/CLEO_QELS.2021.FTu1K.7.

[31] Z.-M. Sheng, J. Zhang, and D. Umstadter, Plasma density gratings induced by intersecting laser pulses in underdense plasmas, Appl. Phys. B **77**, 673 (2003).

[32] L. Friedland and A. Shagalov, Extreme driven ion acoustic waves, Phys. Plasmas **24**, 082106 (2017).

[33] L. Friedland, G. Marcus, J. S. Wurtele, and P. Michel, Excitation and control of large amplitude standing ion acoustic waves, Phys. Plasmas **26**, 092109 (2019).

[34] R. W. Wood, LIII. Phase-reversal zone-plates, and diffraction-telescopes, London, Edinburgh, Dublin Philos. Mag. J. Sci. **45**, 511 (1898).

[35] M. Sussman, Elementary diffraction theory of zone plates, Am. J. Phys. **28**, 394 (1960).

[36] See Supplemental Material at http://link.aps.org/supplemental/10.1103/PhysRevLett.128.065003, which contains [37–46], for simulation details and a note on the scalability of the lenses to large diameters.

[37] S. Tzortzakis, B. Prade, M. Franco, and A. Mysyrowicz, Time-evolution of the plasma channel at the trail of a self-guided IR femtosecond laser pulse in air, Opt. Commun. **181**, 123 (2000).

[38] M. Feit and J. Fleck Jr, Effect of refraction on spot-size dependence of laser-induced breakdown, Appl. Phys. Lett. **24**, 169 (1974).

[39] J. K. Wahlstrand, Y.-H. Cheng, and H. M. Milchberg, Absolute measurement of the transient optical nonlinearity in N_2, O_2, N_2O, and Ar, Phys. Rev. A **85**, 043820 (2012).

[40] M. Mlejnek, E. M. Wright, and J. V. Moloney, Dynamic spatial replenishment of femtosecond pulses propagating in air, Opt. Lett. **23**, 382 (1998).

[41] E. R. Peck and B. N. Khanna, Dispersion of nitrogen, J. Opt. Soc. Am. **56**, 1059 (1966).

[42] A. Couairon, E. Brambilla, T. Corti, D. Majus, O. de J. Ramírez-Góngora, and M. Kolesik, Practitioner's guide to laser pulse propagation models and simulation, Eur. Phys. J. Special Topics **199**, 5 (2011).

[43] C. Guo, M. Li, J. P. Nibarger, and G. N. Gibson, Single and double ionization of diatomic molecules in strong laser fields, Phys. Rev. A **58**, R4271 (1998).

[44] J. Wu, H. Zeng, and C. Guo, Comparison Study of Atomic and Molecular Single Ionization in the Multiphoton Ionization Regime, Phys. Rev. Lett. **96**, 243002 (2006).

[45] A. Talebpour, J. Yang, and S. Chin, Semi-empirical model for the rate of tunnel ionization of N_2 and O_2 molecule in an intense Ti:sapphire laser pulse, Opt. Commun. **163**, 29 (1999).

[46] Z. Song, Z. Zhang, and T. Nakajima, Transverse-mode dependence of femtosecond filamentation, Opt. Express **17**, 12217 (2009).

[47] V. E. Levashov and A. V. Vinogradov, Analytical theory of zone plate efficiency, Phys. Rev. E **49**, 5797 (1994).

[48] P. Yeh, *Introduction to Photorefractive Nonlinear Optics*, Wiley Series in Pure and Applied Optics (Wiley, New York, 1993).

[49] T. Brabec and F. Krausz, Nonlinear Optical Pulse Propagation in the Single-Cycle Regime, Phys. Rev. Lett. **78**, 3282 (1997).

[50] T. D. Arber, K. Bennett, C. S. Brady, A. Lawrence-Douglas, M. G. Ramsay, N. J. Sircombe, P. Gillies, R. G. Evans, H. Schmitz, A. R. Bell, and C. P. Ridgers, Contemporary particle-in-cell approach to laser-plasma modelling, Plasma Phys. Controlled Fusion **57**, 113001 (2015).

Supplemental Material: Holographic Plasma Lenses

M. R. Edwards,[1, *] V. R. Munirov,[2] A. Singh,[2] N. M. Fasano,[3] E. Kur,[1] N. Lemos,[1] J. M. Mikhailova,[3] J. S. Wurtele,[2] and P. Michel[1]

[1]*Lawrence Livermore National Laboratory, Livermore, California 94550*
[2]*University of California at Berkeley, Berkeley, California 94720*
[3]*Princeton University, Princeton, New Jersey 08544*
(Dated: October 28, 2021)

SCALING TO LARGE-DIAMETER LENSES

Plasma lenses have effective damage thresholds for intensity and energy flux, beyond which the probe pulse causes substantial distortion of the lens within its own duration. Although these intensity and flux limits for both ionization and ponderomotive lenses are much higher than those for a solid optic, manipulating pulses with very high powers and energies using a plasma optic requires expanding the lens diameter. Intensity and energy-flux driven damage of the plasma is primarily a local effect, so the total power and energy tolerance of an optic will increase proportionally to area.

Figure 1 shows a 3D paraxial simulation of a probe beam being focused by a 5-mm-diameter plasma lens. In this case, a high-quality focal spot is produced at a focal length of 8 mm from a probe beam originally focused at $z = 48$ mm, demonstrating that this type of zone-plate optic can be created with mm-scale diameter.

The SVI optic shown in Fig. 4ab of the manuscript has an energy-flux limit of 230 J/cm^2 and the ponderomotive optic described in Fig. 4cd has an intensity limit around 2×10^{17} W/cm^2. Applying these limits to a plasma lens with 5 mm diameter, as shown in Fig. 1, would allow a 5-mm SVI plasma lens to focus a 45 J pulse and a 5-mm ponderomotive lens to focus a 40 PW laser pulse. Millimeter-scale ponderomotive lenses can therefore be used to control the highest power lasers pulse available today.
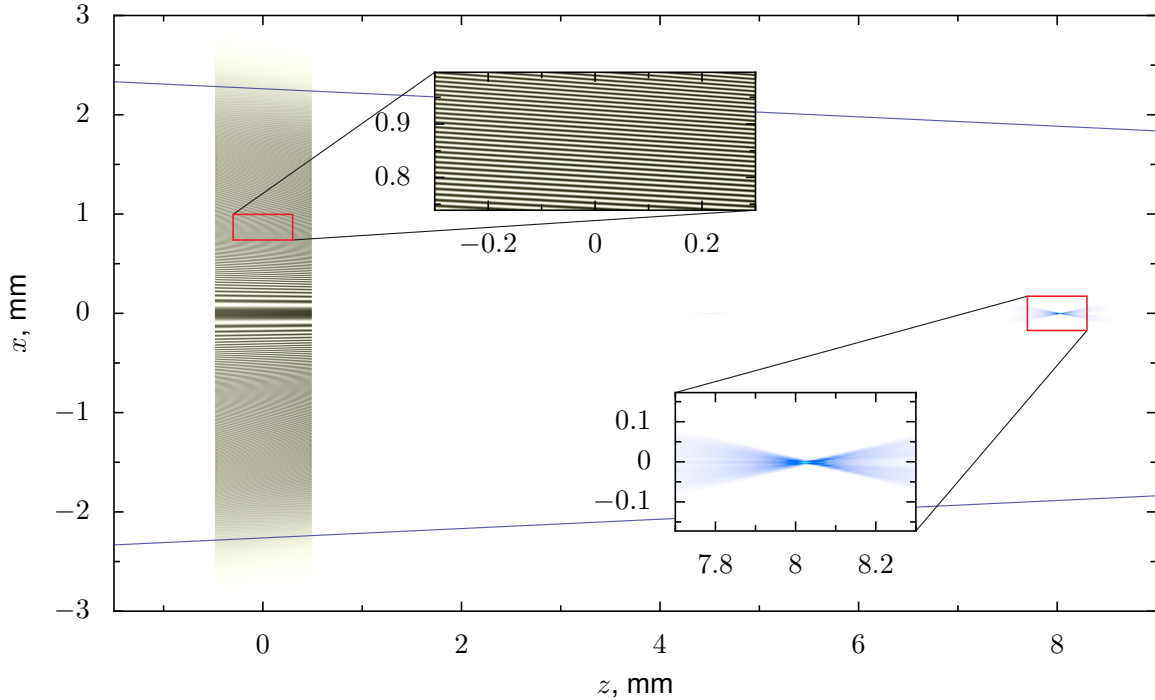

FIG. 1. Three dimensional calculation of focusing by a 5-mm-diameter plasma lens (grayscale) formed in a 1-mm thick plasma by two pump beams ($f_A = 8$ mm, $f_B = 48$ mm). The probe beam, which is incident with a focus at $z = 48$ mm, is brought to a focus at 8 mm by the lens (blue). The blue solid lines show the edges of the probe beam propagation if not affected by the lens.

SIMULATION DETAILS

Paraxial Propagation Solver

The paraxial propagation solver (Figs. 2 and 3) solves the paraxial wave equation in the presence of an index modulation for a single-frequency infinite-duration beam:

$$(2ik_0\partial_z + \nabla_\perp^2)E(\boldsymbol{r}) = -2k_0^2 E(\boldsymbol{r})\frac{\delta n(\boldsymbol{r})}{n_0}, \tag{1}$$

where the electric field ($\tilde{E}$) is decomposed into envelope and high-frequency components as $\tilde{E}(\boldsymbol{r},t) = \frac{1}{2}E(\boldsymbol{r})\exp[i(k_0 z - \omega_0 t)] + \text{c.c.}$, k_0 is the wavenumber, ω_0 is the frequency, and $\mathbf{r}$ is the vector position. In our calculations, this equation is first evaluated for the pump beams, and an index modulation left by the pumps is calculated via $\delta n = f(E)$. For the results presented in this paper, $f(E) \propto |E|^q$ with $q = 4$ (Fig. 2, Fig. 3a) or $q = 2$ (Fig. 3bc). The probe beam is then propagated according to Eq. 1 through the distribution of δn left by the pump beams. This approach does not resolve the time dynamics of plasma formation or the self-action via medium nonlinearity for the pumps or probe, but does allow efficient evaluation of the performance of arbitrary volumetric diffractive optics in the linear regime, which is where a plasma optic would be designed to operate. Parameters for simulations reported in this paper are presented in Table I.

TABLE I. Parameters for the Paraxial Propagation Solver

Parameter	Symbol	Fig. 2a	Fig. 2b	Fig. 2c	Fig. SM1	Units
Pump wavelength	λ_p	400	800	800	800	nm
Pump focal position [A, B][a]	$[f_A, f_b]$	[6, 1]	[3, 0.5]	[3, 0.5]	[48, 8]	mm
Pump divergence [A, B]	$[\theta_A, \theta_B]$	[1, 6]	[2, 12]	[2, 12]	[3, 18]	°
Probe wavelength	λ_0	400	800	800	800	nm
Probe focal position	f_0	1	3	3	48	mm
Probe divergence	θ_0	6	1.8	1.8	2.7	°
Maximum index modulation	Δn	1.3×10^{-4}	3.3×10^{-3}	$[10^{-5} - 0.009]$	6.6×10^{-4}	-
Initial medium extent	D	1000	200	200	1000	μm
Modulation formation exponent[b]	q	4	2	2	2	-
Transverse spatial resolution	$\Delta x, \Delta y$	120	160	160	868	nm
Transverse spatial extent	-	551	277	277	6000	μm
Transverse grid points	N_x, N_y	4608	1728	1728	6912	-
Longitudinal resolution, medium	Δz	50	5	5	25	μm
Longitudinal grid points, medium	N_z	20	40	40	40	-

[a] In z, where $z = 0$ is at the center of the plasma. The plasma extends from $z = -D/2$ to $z = D/2$.
[b] This is the parameter q, where $\delta n = |E|^q$.

Nonlinear Envelope Equation Solver

The nonlinear envelope equation solver calculates the propagation of a light pulse under the paraxial and slowly varying envelope approximations. With the inclusion of nonlinear terms for plasma phase shift and absorption, ionization losses, and Kerr self-focusing, the governing equation is [7]:

$$\frac{\partial E}{\partial z} = \frac{i}{2k}\nabla_\perp^2 E - \frac{ik''}{2}\frac{\partial^2 E}{\partial t^2} - \frac{\sigma}{2}(1 + i\omega\tau)n_e E - W_{FI}(E)n_N\frac{U_i}{2|E|^2} + ik_0 n_2^T\left[(1-f)|E|^2 + f\int_{-\infty}^{\infty}R(t-t')|E(t')|^2 dt'\right] \tag{2}$$

where the first term on the right hand side is the usual paraxial diffraction term and the second term represents group velocity dispersion ($k'' = d^2k/d\omega^2$). Note that the electric field here is assumed to be in the units of the square root of intensity. We use the following dispersion relation for nitrogen [8], where $k_{[\mu m^{-1}]}$ is the wavenumber in

TABLE II. Parameters for the Nonlinear Envelope Equation Solver (Fig. 3ab, Fig. 4a)

Parameter	Symbol	Value	Units	Reference
Pump central wavelength	λ_p	800	nm	
Pump duration[a]	τ_p	10	fs	
Pump focal position [A, B][b]	$[f_A, f_b]$	[3, 0.5]	mm	
Pump divergence [A, B]	$[\theta_A, \theta_B]$	[2, 12]	°	
Pump energy [A, B]	-	[0.65, 0.65]	mJ	
Probe central wavelength	λ_0	800	nm	
Probe duration	τ_0	1	ps	
Probe focal position	f_0	3	mm	
Probe divergence	θ_0	1.5	°	
Probe energy	-	60 [1-1000]	mJ	
Probe delay[c]	$\Delta\tau$	0.8	ps	
Neutral species	-	N_2	-	
Permitted ionized species	-	N_2^+	-	
Ionization energy	U_i	15.58	eV	
Initial neutral number density	$n_{N,0}$	2.5×10^{19}	cm^{-3}	
Initial neutral extent	D	200	μm	
Recombination parameter	a	1.2×10^{-13}	m^3/s	[3][d]
Collision frequency[e]	τ_0	3.5×10^{-13}	s^{-1}	[4, 5]
Instantaneous neutral nonlinearity	n_2	7.4×10^{-24}	cm^2/W	[6][f]
Delayed response fraction	f	0.77	-	[6]
Transverse spatial resolution, vacuum[g]	$\Delta x, \Delta y$	340	nm	
Transverse spatial extent, vacuum	-	0.7	mm	
Transverse grid points, vacuum	N_x, N_y	2048	-	
Transverse spatial resolution, non-vacuum	$\Delta x, \Delta y$	340	nm	
Transverse spatial extent, non-vacuum	-	0.35	mm	
Transverse grid points, non-vacuum	N_x, N_y	1024	-	
Longitudinal spatial resolution, non-vacuum	Δz	1	μm	
Longitudinal grid points, non-vacuum	N_z	200		
Temporal resolution, pumps	Δt	0.31	fs	
Temporal extent, pumps	-	20	fs	
Temporal grid points, pumps	N_t	64	-	
Temporal resolution, probe	Δt	39	fs	
Temporal extent, probe	-	2.5	ps	
Temporal grid points, probe	N_t	64	-	

[a] Pulse durations are given in terms of the full-width-half-maximum (FWHM) of the Gaussian intensity envelope in time.
[b] In z, where $z = 0$ is at the center of the plasma.
[c] Delay is the time separation between the peak of the pump pulses and the peak of the probe pulse.
[d] Also close to the value 1×10^{-13} m^3/s from [4], where we have used values measured in air.
[e] For fully non-ionized conditions. The collision frequency is recalculated locally as neutral density changes.
[f] Due to the relatively short length of the propagation distance in the neutral medium, we do not observe a strong dependence on the exact value of this parameter for the performance of the optic.
[g] The simulation is divided into vacuum and non-vacuum components, where vacuum propagation can be spectrally solved for arbitrary propagation distance in a single step, and the non-vacuum propagation must be calculated with finite steps in z due to the medium response. The larger diameters of the beams outside the plasma requires a larger transverse size for the simulations.

radians/micron:

$$n(k) = 1 + \frac{5.1097029 \times 10^{-2}}{183.69459 - (k_{[\mu m^{-1}]}/2\pi)^2} + \frac{2.12949 \times 10^{-6}}{7.74396 + (k_{[\mu m^{-1}]}/2\pi)^2}. \tag{3}$$

The third term on the right hand side of Eq. 2 represents the phase shift and absorption by free electrons (density n_e), where the inverse Bremsstrahlung cross section (σ) is calculated locally with:

$$\sigma = \frac{ke^2\tau}{\omega m_e \varepsilon_0 (1 + \omega^2\tau^2)}. \tag{4}$$

The electron mass and charge are e and m_e, respectively, and ε_0 is the vacuum permittivity. The collision time τ is calculated based on local neutral density.

The fourth term represents loss of energy to the formation of the plasma, where W_{FI} is the field ionization rate and U_i is the ionization energy, and the fifth term contains both the instantaneous $[n_2 = (1 - f)n_2^T]$ and time delayed contributions to the Kerr nonlinearity. Here, f is the relative contribution of the delayed component to the total n_2^T. The delayed response is approximated with a damped harmonic oscillator model [7]:

$$R(t) = H(t)\Omega^2 e^{-\Gamma t/2} \frac{\sin\left(t\sqrt{\Omega^2 - \Gamma^2/4}\right)}{\sqrt{\Omega^2 - \Gamma^2/4}} \tag{5}$$

where H is the Heaviside step function and, following [7] for air, we have taken $\Gamma = 26$ THz and $\Omega = 20.6$ THz.

The free electron density n_e evolves according to [9]:

$$\frac{\partial n_e}{\partial t} = W_{\text{FI}}(E)n_N + W_{\text{Ava}}(E)n_e - an_e^2. \tag{6}$$

where W_{FI} is the rate of field ionization, W_{Ava} is the rate of collisional (avalanche) ionization, and a is the recombination parameter. Since we consider here a single neutral species (N_2) and a single ionized species (N_2^+), the time derivative of the neutral density (n_N) is simply:

$$\frac{\partial n_N}{\partial t} = -\frac{\partial n_e}{\partial t}, \tag{7}$$

and the initial neutral density is $n_{N,0}$. The rate of collisional ionization is:

$$W_{\text{Ava}} = \frac{\sigma}{U_i}|E|^2 \tag{8}$$

Note that we assume the electrons do not change position once formed, and the condition that the plasma remains frozen at the position of its formation sets a limit on the longest pulses and delay times that can be considered with this model.

For the parameters we consider here, the Keldysh parameter is in an intermediate regime, so to determine the field ionization rate we use the Perelomov, Popov, and Terentev (PPT) model with semi-empirical corrections based on experimental data [10–12]. The photoionization rate due to field ionization $W_{\text{FI}}(I)$ in the PPT model is given, using atomic units, by [13]

$$W_{\text{FI}}(I) = \sqrt{\frac{6}{\pi}}|C_{n^*l^*}|^2 f_{lm}U_i \left[\frac{2(2U_i)^{\frac{3}{2}}}{F}\right]^{2n*-|m|-\frac{3}{2}} \left(1 + \gamma^2\right)^{\frac{|m|}{2} + \frac{3}{4}} A_m(\omega, \gamma) \exp\left[-\frac{2g(\gamma)(2U_i)^{\frac{3}{2}}}{3F}\right], \tag{9}$$

where $n^* = Z/\sqrt{2U_i}$, $l^* = n^* - 1$, Z is the ion charge, U_i is the ionization potential, F is the peak laser electric field (laser intensity $I = 3.51 \times 10^{16}$ W/cm^2 for $F = 1$ au), and

$$|C_{n^*l^*}|^2 = \frac{2^{2n^*}}{n^*\Gamma(n^* + l^* + 1)\Gamma(n^* - l^*)}, \tag{10}$$

where Γ represents the gamma function,

$$f_{lm} = \frac{(2l + 1)(l + |m|)!}{2^{|m|}|m|!(l - |m|)!}, \tag{11}$$

$$g(\gamma) = \frac{3}{2\gamma}\left[\left(1 + \frac{1}{2\gamma^2}\right)\sinh^{-1}(\gamma) - \frac{\sqrt{1 + \gamma^2}}{2\gamma}\right], \tag{12}$$

$$A_m(\omega, \gamma) = \frac{4}{\sqrt{3\pi}}\frac{1}{|m|!}\frac{\gamma^2}{1 + \gamma^2}\sum_{n>v}^{\infty} e^{-(n-v)\alpha(\gamma)}w_m\left(\sqrt{\frac{2\gamma(n - v)}{\sqrt{1 + \gamma^2}}}\right), \tag{13}$$

$$w_m(x) = e^{-x^2} \int_0^x \left(x^2 - y^2\right)^{|m|} e^{y^2} dy, \tag{14}$$

$$\alpha(\gamma) = 2\left[\sinh^{-1}(\gamma) - \frac{\gamma}{\sqrt{1+\gamma^2}}\right], \tag{15}$$

$$v = \frac{E_i}{\omega}\left(1 + \frac{1}{2\gamma^2}\right), \tag{16}$$

$$\gamma = \frac{\omega\sqrt{2U_i}}{F} = \frac{\omega Z}{Fn^*} = \frac{\omega F_0^{\frac{1}{3}}}{F} \tag{17}$$

where $F_0 = (2U_i)^{\frac{3}{2}}$.

For O_2 and N_2 we take $l = m = 0$. Thus, we have

$$W_{\mathrm{FI}}(I) = \sqrt{\frac{6}{\pi}}\,|C_{n^*l^*}|^2\,f_{00}U_i\left[\frac{2\,(2U_i)^{\frac{3}{2}}}{F}\right]^{2n^*-\frac{3}{2}}\left(1+\gamma^2\right)^{\frac{3}{4}} A_0(\omega,\gamma)\exp\left[-\frac{2g(\gamma)\,(2U_i)^{\frac{3}{2}}}{3F}\right], \tag{18}$$

$$f_{00} = 1, \tag{19}$$

$$A_0(\omega,\gamma) = \frac{4}{\sqrt{3\pi}}\frac{\gamma^2}{1+\gamma^2}\sum_{n=[v]+1}^{\infty} e^{-(n-v)\alpha(\gamma)}w_0\left(\sqrt{\frac{2\gamma\,(n-v)}{\sqrt{1+\gamma^2}}}\right), \tag{20}$$

$$w_0(x) = e^{-x^2}\int_0^x e^{y^2}dy = \frac{\sqrt{\pi}}{2}e^{-x^2}\mathrm{erfi}(x), \tag{21}$$

where erfi is the imaginary error function. Following [12], for nitrogen N_2 and an 800 nm laser we take $U_i = 15.58$ eV and $Z_{\mathrm{eff}} = 0.9$.

We numerically evaluate Eq. 2 separately for the pumps and the probe using a standard method in reference frames that move with the group velocity of light [9]. Each pulse is specified in two transverse spatial dimensions and time; the distribution of light in transverse space and time is then updated by stepping through the propagation direction (z). To account for the delayed probe, we have extended the standard treatment by solving Eq. 2 twice: once for the pump beams propagating in the initial neutral gas, and a second time for the probe. The probe solution takes as an initial condition the plasma distribution left after the pump, evolved according to Eq. 6 over the time delay between the pump and probe. The computational and physical parameters used for the simulations shown in Fig. 4ab are given in Table II.

Since the two parts of this calculation are connected only by the initial condition on the plasma distribution for the second part, we can use different time resolution for the pump and probe calculations. In vacuum regions, both the pumps and the probe can be propagated linearly over arbitrary distances, allowing a somewhat higher number of spatial grid points without prohibitive computational cost. Table II specifies the resolution and number of grid points used for time and all three dimensions of space, distinguishing where necessary between the pump and probe and between vacuum and non-vacuum propagation.

Particle-in-Cell

Two-dimensional (2D) particle-in-cell (PIC) simulations were conducted with the code EPOCH [14] to study the formation of an ion-wave plasma lens in a fully ionized initial plasma and its tolerance of high probe intensity (Figure 4e). The simulation box was 300 μm long and 150 μm wide (9000×4500 cells), containing the plasma lens and the probe focal spot. All lasers were introduced at the left boundary ($z = -21$ μm) with gaussian temporal profiles and supergaussian (order 4) spatial profiles. The pumps and probe were all polarized in the x direction, i.e. their electric

TABLE III. 2D PIC Simulation Parameters (Fig. 4b)

Parameter	Symbol	Value	Units
Pump wavelength	λ_p	1000	nm
Pump duration[a]	τ_p	500	fs
Pump focal position [A, B][b]	$[f_A, f_b]$	[8, 0.2]	mm
Pump divergence [A, B]	$[\theta_A, \theta_B]$	[0.35, 14]	°
Pump peak power [A, B]	-	[15, 15]	TW
Probe wavelength	λ_0	1000	nm
Probe duration	τ_0	40	fs
Probe focal position	f_0	8	mm
Probe divergence	θ_0	0.3	°
Probe peak power	-	$10^{10} - 10^{18}$	W
Probe delay[c]	$\Delta\tau$	1.2	ps
Plasma density	n_e	5×10^{19}	cm^{-3} [d]
Plasma extent	D	40	μm
Electron temperature	T_e	100	eV
Ion temperature	T_i	10	eV
Ion mass (atomic hydrogen)	m_i	1836	m_e [e]
Spatial resolution	$\Delta x, \Delta z$	40	nm [f]
Temporal resolution	Δt	0.090	fs [g]
Particles per cell per species	-	10	-
Spatial extent, longitudinal	-	45	μm
Spatial extent, transverse	-	135	μm

[a] Pulse durations are given in terms of the full-width-half-maximum (FWHM) of the Gaussian intensity envelope in time.
[b] In z, where $z = 0$ is at the center of the plasma.
[c] Delay is the time separation between the peak of the pump pulses and the peak of the probe pulse.
[d] $N = n_e/n_c = 0.045$.
[e] In units of the electron mass, m_e.
[f] $\lambda_0/\Delta x = 25$.
[g] $\Delta t = 0.95\Delta x/(\sqrt{2}c)$.

fields were within the 2D plane of the simulation. The simulation captured the creation of the lens by the pumps, the evolution of the plasma between the pumps and the probe, and the interaction of the probe beam with the plasma. The physical and computational parameters used for the PIC simulations are given in Table III.

We also conducted three-dimensional particle-in-cell simulations (Fig. 4cd), showing the full performance of an ion-wave plasma lens. These simulations were conducted with the same physical parameters as used for the 2D simulations, but with reduced spatial resolution and simulation size. A moving window was used, which remained stationary on the plasma as the pump beams formed the lens, but moved with the probe beam after it left the plasma, staying with through the focus. The parameters for the 3D PIC simulations are provided in Fig. IV.

---

[*] edwards78@llnl.gov

[1] J. Kirz, Phase zone plates for x rays and the extreme uv, J. Opt. Soc. Am. **64**, 301 (1974).
[2] R. W. Wood, LIII. Phase-reversal zone-plates, and diffraction-telescopes, Lond. Edinb. Dubl. Phil. Mag. **45**, 511 (1898).
[3] S. Tzortzakis, B. Prade, M. Franco, and A. Mysyrowicz, Time-evolution of the plasma channel at the trail of a self-guided IR femtosecond laser pulse in air, Opt. Commun. **181**, 123 (2000).
[4] M. Feit and J. Fleck Jr, Effect of refraction on spot-size dependence of laser-induced breakdown, Appl. Phys. Lett. **24**, 169 (1974).
[5] A. Couairon and A. Mysyrowicz, Femtosecond filamentation in transparent media, Phys. Rep. **441**, 47 (2007).
[6] J. Wahlstrand, Y.-H. Cheng, and H. Milchberg, Absolute measurement of the transient optical nonlinearity in N_2, O_2, N_2O, and Ar, Phys. Rev. A **85**, 043820 (2012).
[7] M. Mlejnek, E. M. Wright, and J. V. Moloney, Dynamic spatial replenishment of femtosecond pulses propagating in air, Opt. Lett. **23**, 382 (1998).
[8] E. R. Peck and B. N. Khanna, Dispersion of nitrogen, J. Opt. Soc. Am. **56**, 1059 (1966).

TABLE IV. 3D PIC Simulation Parameters (Fig. 3cd)

Parameter	Symbol	Value	Units
Pump wavelength	λ_p	1000	nm
Pump duration[a]	τ_p	500	fs
Pump focal position [A, B][b]	$[f_A, f_b]$	[8, 0.2]	mm
Pump divergence [A, B]	$[\theta_A, \theta_B]$	[0.35, 14]	°
Pump peak power [A, B]	-	[15, 15]	TW
Probe wavelength	λ_0	1000	nm
Probe duration	τ_0	40	fs
Probe focal position	f_0	8	mm
Probe divergence	θ_0	0.3	°
Probe peak power	-	100	TW
Probe delay[c]	$\Delta\tau$	1.2	ps
Plasma density	n_e	5×10^{19}	cm^{-3} [d]
Plasma extent	D	40	μm
Electron temperature	T_e	100	eV
Ion temperature	T_i	10	eV
Ion mass (atomic hydrogen)	m_i	1836	m_e [e]
Spatial resolution	$\Delta x, \Delta y, \Delta z$	71.4	nm [f]
Temporal resolution	Δt	0.013	fs [g]
Particles per cell per species	-	2	-
Spatial extent, longitudinal	-	45	μm
Spatial extent, transverse	-	135	μm

[a] Pulse durations are given in terms of the full-width-half-maximum (FWHM) of the Gaussian intensity envelope in time.
[b] In z, where $z = 0$ is at the center of the plasma.
[c] Delay is the time separation between the peak of the pump pulses and the peak of the probe pulse.
[d] $N = n_e/n_c = 0.045$.
[e] In units of the electron mass, m_e.
[f] $\lambda_0/\Delta x = 14$.
[g] $\Delta t = 0.95\Delta x/(\sqrt{3}c)$.

[9] A. Couairon, E. Brambilla, T. Corti, D. Majus, O. de J. Ramírez-Góngora, and M. Kolesik, Practitioner's guide to laser pulse propagation models and simulation, Eur. Phys. J. Spec. Top. **199**, 5 (2011).

[10] C. Guo, M. Li, J. P. Nibarger, and G. N. Gibson, Single and double ionization of diatomic molecules in strong laser fields, Phys. Rev. A **58**, R4271 (1998).

[11] J. Wu, H. Zeng, and C. Guo, Comparison study of atomic and molecular single ionization in the multiphoton ionization regime, Phys. Rev. Lett. **96**, 243002 (2006).

[12] A. Talebpour, J. Yang, and S. Chin, Semi-empirical model for the rate of tunnel ionization of N_2 and O_2 molecule in an intense Ti:sapphire laser pulse, Opt. Commun. **163**, 29 (1999).

[13] Z. Song, Z. Zhang, and T. Nakajima, Transverse-mode dependence of femtosecond filamentation, Opt. Express **17**, 12217 (2009).

[14] T. D. Arber, K. Bennett, C. S. Brady, A. Lawrence-Douglas, M. G. Ramsay, N. J. Sircombe, P. Gillies, R. G. Evans, H. Schmitz, A. R. Bell, and C. P. Ridgers, Contemporary particle-in-cell approach to laser-plasma modelling, Plasma Phys. Contr. F. **57**, 113001 (2015).